Water-anchored edge defects in amorphous carbon probed with thermal- and electro-assisted Raman spectroscopy and nanoscopy

Sergey S. Kharintsev[1*], Svetlana V. Saparina[1], Alexandr I. Fishman[1], Andrei A. Stolov[2] and Jie Li[2]

[1]Department of Optics and Nanophotonics, Institute of Physics, Kazan Federal University, Kremlevskaya, 16, Kazan, 420008, Russia

[2]OFS, 55 Darling Drive, Avon, CT, 06001, USA

*To whom correspondence should be addressed. E-mail: (S.S.K.) Sergey.Kharintsev@kpfu.ru

KEYWORDS: optical fiber, functionalized edge defects, carbon coating, tip-enhanced Raman scattering, depolarizarion, dc conductivity, scanning thermal microscopy, polarization-controlled Raman spectroscopy, electro-assisted TERS spectroscopy, water on graphite, carboxyl, hydroxyl.

ABSTRACT

As-thermal-CVD-synthesized amorphous carbon (a-C) ultrathin coatings enable silica optical fibers be mechanically robust and optically transparent in aggressive environments. This is achieved by mitigating both hydrogen diffusion and water ingression onto the fiber surface. Notwithstanding the advanced performance of CVD-deposited a-C films, their functionality may suffer from structural and topology defects, dopants, intrinsic stresses and other imperfections. In this paper, we experimentally study the influence of water-anchored edge functional groups on dc electrical conductivity and Raman scattering of a-C films, ranging from 10 to 100 nm in thickness, exposed to thermal and electrical annealing. A series of heating/cooling cycles was found to affect

the disorder *D*-family bands in the Raman spectra of a-C. In particular, two new Raman peaks at 1260 cm^{-1} and 1400 cm^{-1}, attributed to carboxyl (COOH) and hydroxyl (C-OH) groups, have been unraveled through polarization-controlled far-field Raman spectroscopy and tip-enhanced Raman scattering (TERS) spectroscopy. The TERS technique allows one to readily resolve the broad disorder *D*-family bands due to the excitation of coherent Raman scatters (nano-sized graphitic clusters). A temperature-sensitive and thickness-dependent hysteresis in dc conductivity, observed at temperatures of above 80°C, is explained by physical sorption/desorption of water at the surface of graphite-like crystals through hydrogen bonding and dissociative absorption of water with the formation of extra COOH/C-OH groups at the edge defects. The electro-heating leads to a non-uniform distribution of the water-decorated edges owing to hot spots of a percolated carbon crystals network. This is directly evidenced by electro-assisted TERS mapping of the a-C coating. We believe that our study will pave a way into the understanding of how water interacts with amorphous carbon and improve the performance of carbon coatings in harsh environments.

Introduction

Amorphous carbon (a-C), containing mixed sp^2/sp^3 species, serves as one of the base materials for developing fiber optical sensing and telecommunication systems.[1,2] In practice, carbon-coated optical fibers are often exploited within a wide range of temperature and/or pressure and are exposed to water and other aggressive chemicals from the surrounding environment.[1] The a-C coatings, usually formed through thermal chemical vapor deposition (TCVD), create a barrier to hydrogen and water and this way allow the optical fibers to remain mechanically robust and optically transparent even at harsh conditions. There was previously believed that a-C coatings represent a disordered network of nano-sized graphitic platelets with many micro-voids that provide pathways for the diffusion of hydrogen and water.[3] Depending on the TCVD conditions,

deposited a-C coatings may contain a diversity of carbon allotropes such as graphene/graphene oxide sheets (or molecules),[4–6] zipped/unzipped graphene nanotubes/nanoribbons,[7,8] fullerenes,[9] nanohors,[10] carbon quantum dots,[11] graphite tubules,[12] to name a few. Compared to the higher-order structures, amorphous carbon contains a huge amount of structural/topological defects on a basal plane and at the edges, typically 10^{17}-10^{20} cm^{-3},[13,14] depending on the preparation conditions. These include armchair/zigzag edge defects, mono-vacancies and multi-vacancies, adatoms, pentagon-heptagon pair defects (sometimes referred to as Stone-Wales defects) and other Haeckelite disordered structures.[15–17] The presence of single pentagon or heptagon defects leads to the formation of a positive and negative curvature of a graphene sheet, making it 'crumpled' to minimize free Gibbs energy. Even a defect-free graphene sheet was found to be permeable to hydrogen but not to other gases and liquids.[18] The permeability and chemical reactivity are enhanced with the formation of ripples on a-C film surface. It is well established, that the defects are able to chemically interact with the H_2 and H_2O molecules and their dissociative constituents: H^+ and OH^-.[19–22] The enrichment of graphite-like crystals with such functional groups as C-H, COOH/C-OH and C=O/C-O can noticeably change mechanical, electrical and optical properties of the a-C thin films.[23] The chemical functionalization leads to the appearance of sp^3 hybridized C-C bonds and, eventually, it makes carbon material amorphous. Physical and chemical properties of carbon allotropes decorated with the functional groups are comprehensively reviewed in the literature. Most attention has been paid to covalent functionalization of graphene and other related carbon allotropes.[24] The functional groups themselves are capable of interaction with water from the atmosphere through hydrogen bonding mechanism. To the best of our knowledge, water-anchored edge defects of graphite-like crystals are poorly understood. We can assume that multiple mild heating/cooling cycles within the range of 20°C-200°C make a-C coatings better hermetic and hard due to tamping of randomly oriented graphite-like nano-crystals. However, the rearrangement of the nano-crystals must take a place regardless of the environment. As will be shown below, the

temperature-dependent dc electrical resistance of a-C coatings exhibits different behaviors in air vs. low vacuum. A hysteresis of dc electrical resistance of the a-C is experimentally observed at cyclic heating/cooling within the temperature range of 30°C-150°C. This hysteresis was found to be related to the water-enriched/depleted edge defects and can be directly followed by using far- and near-field Raman spectroscopy and nanoscopy.

Despite the fact that far-field Raman spectra of carbon materials are well studied, the intrinsic content of a broad Raman band within the spectral range of 1000-2000 cm^{-1} is still under debate. Depending on the structure of carbonaceous material, a multi-peak fitting analysis allows one to decompose a broad Raman spectrum into four,[11,15] five[25–27] or even six[24] elementary peaks. Following to the Occam's razor principle, the use of additional *a priori* information on a sought solution must be justified by the nature rather than a desire to fit Raman spectra with a minimal total discrepancy. In the simplest case, any imperfect graphitic material exhibits two characteristic bands indicated as *G* and *D*.[28] The *G* peak, normally observed at 1575 cm^{-1}, originates from the in-plane vibration of sp^2 carbon atoms and corresponds to a doubly degenerate (TO and LO) phonon mode with E_{2g} symmetry. For the amorphous carbon the *G* band is red-shifted to 1550 cm^{-1}. The *D* band at 1360 cm^{-1}, attributed to in plane (LA) armchair/zigzag edge defects with symmetry A_{1g}, is due to the first-order double resonance Raman scattering process. This disorder mode is Raman active for small crystallites or boundaries of larger crystals. The intensity of this mode is inversely proportional to the effective crystallite size L_a in the direction of the graphene plane. With the advent of structural/topological defects, a new disordered peak *D*' (E_{2g} symmetry) appears at 1620 cm^{-1}. This mode is commonly inactive and may be activated though phonon confinement due to the structural defects. By analogy to the *D* band, the *D*' band is consistent with defect-induced double resonance Raman theory. Both the *D* and *D*' bands are related to the inter-valley and intra-valley scatterings around the *K* point of the first Brillion zone, respectively.[15] Along with the considered bands, an additional peak (D^*) at 1470 cm^{-1} appears due to the covalent attachment of

oxygen (C=O/C-O) to the edges and the formation of the sp^2-sp^3 bonds. In addition, there is a low-frequency broad band *D*" at 1130 cm^{-1}, that makes the wing of the disorder *D* band highly asymmetric, can be attributed to the sp^2-sp^3 bonds or C–C and C=C stretching vibrations of polyene-like structures.[25,29] A closer examination of Raman spectra of functionalized carbon-related materials reported previously[11,26] clearly indicated a need of exploiting more for better fitting the experimental data. In particular, one can see two latent specific bands at 1260 cm^{-1} and 1400 cm^{-1} in the *D*-region of the Raman spectra. Their assignment to specific vibrational modes is not a trivial task because these may be caused by both the structural defects and/or attached functional groups.[4,20,21,24] Recent theoretical studies have claimed that the bands at 1260 cm^{-1} and 1400 cm^{-1} could be assigned to COOH/C-OH groups.[20,24] However, this hypothesis has not been supported by experimental investigations so far.

In this paper, we investigate an anomalous thickness-dependent hysteresis of the dc electrical resistance of a-C thin films observed upon mild heating/cooling cycles in ambient air. This effect is explained by physical sorption/desorption of water at COOH/C-OH functional groups attached to a-C. The sorption/desorption is implemented via hydrogen bonding at temperatures of above 80^{o}C. This conclusion is confirmed by the observed rearrangements of Raman peaks at 1260 cm^{-1} and 1400 cm^{-1} registered through polarization-controlled far-field Raman spectroscopy. Further evidence is provided using tip-enhanced Raman scattering (TERS) spectroscopy, where the broad disorder D-family band is resolved into individual components due to the excitation of coherent Raman scatters (nano-sized graphitic clusters). The electro-assisted TERS spectra clearly reveal two Raman peaks at 1260 cm^{-1} and 1400 cm^{-1}, assigned to carboxyl (-COOH) and hydroxyl (-OH) groups attached to the edge sites of graphite crystals. By heating above 80^{o}C, the intercalated water species partially desorb and leave the crystal. At the same time, the water species adsorbed at the edge defects undergo the dissociative absorption with the formation of the COOH/C-OH groups. It is important to note that the hermeticity of most carbonaceous materials deteriorates with the

concentration of the edge defects which are further functionalized with water.[20] Upon cooling, the graphite-like crystals are water enriched through the attachment of the H_2O molecules to the edge functional groups. Eventually, the electrical resistance increases irreversibly, and the strength of the effect was found to depend upon the coating thickness. This is followed by a decrease of the total intensity of electro-assisted TERS bands within the OH stretching spectral range of 3100-3500 cm^{-1}.

Results and discussion

The carbon coating used in our study was applied by pulling hot (800-1000°C) silica optical fibers though a TCVD reactor. The precursor hydrocarbon gas was cracked to form carbonaceous species at the curved surface of the silica glass fiber. The fiber diameter *D* was 125 μm. The a-C coatings were designed for preventing hydrogen and water ingression onto the fiber surface. Protective properties of the a-C are straightforwardly related to its intrinsic molecular structure and the coating thickness. The a-C layer thickness, *h*, controlled by the precursor gas flow rate and the silica fiber temperature, was roughly evaluated by the following relationship

$$h = \frac{\rho}{\pi D R}, \qquad (1)$$

where R is the electrical resistance ($k\Omega \cdot cm^{-1}$) to be directly measured and ρ is the carbon material resistivity. Despite the fact that the resistivity, ρ, for carbonaceous materials varies from $0.39 \cdot 10^{-4}\ \Omega \cdot cm$ (graphite species) to $60 \cdot 10^{-4}\ \Omega \cdot cm$ (amorphous species), in our study we assumed the magnitude of $17.6 \cdot 10^{-4}\ \Omega \cdot cm$ which was determined previously for a similar fiber.[30] Three carbon-coated fibers were prepared with the a-C thicknesses of 12.2 nm, 31nm and 107 nm. As it was shown in our previous study,[26] the degree of crystallinity of a-C increases with the coating thickness within the range of 0-50 nm and begins to decline monotonically beyond this range. In

other words, the average size of a graphitic crystal reaches the maximum at the thickness of ca. 40-60 nm and further it becomes unchangeable. The electrical and spectroscopic properties depend upon the orientation of the crystallites and their perfection. Fig. 1 (a) and (b) shows two experimental setups

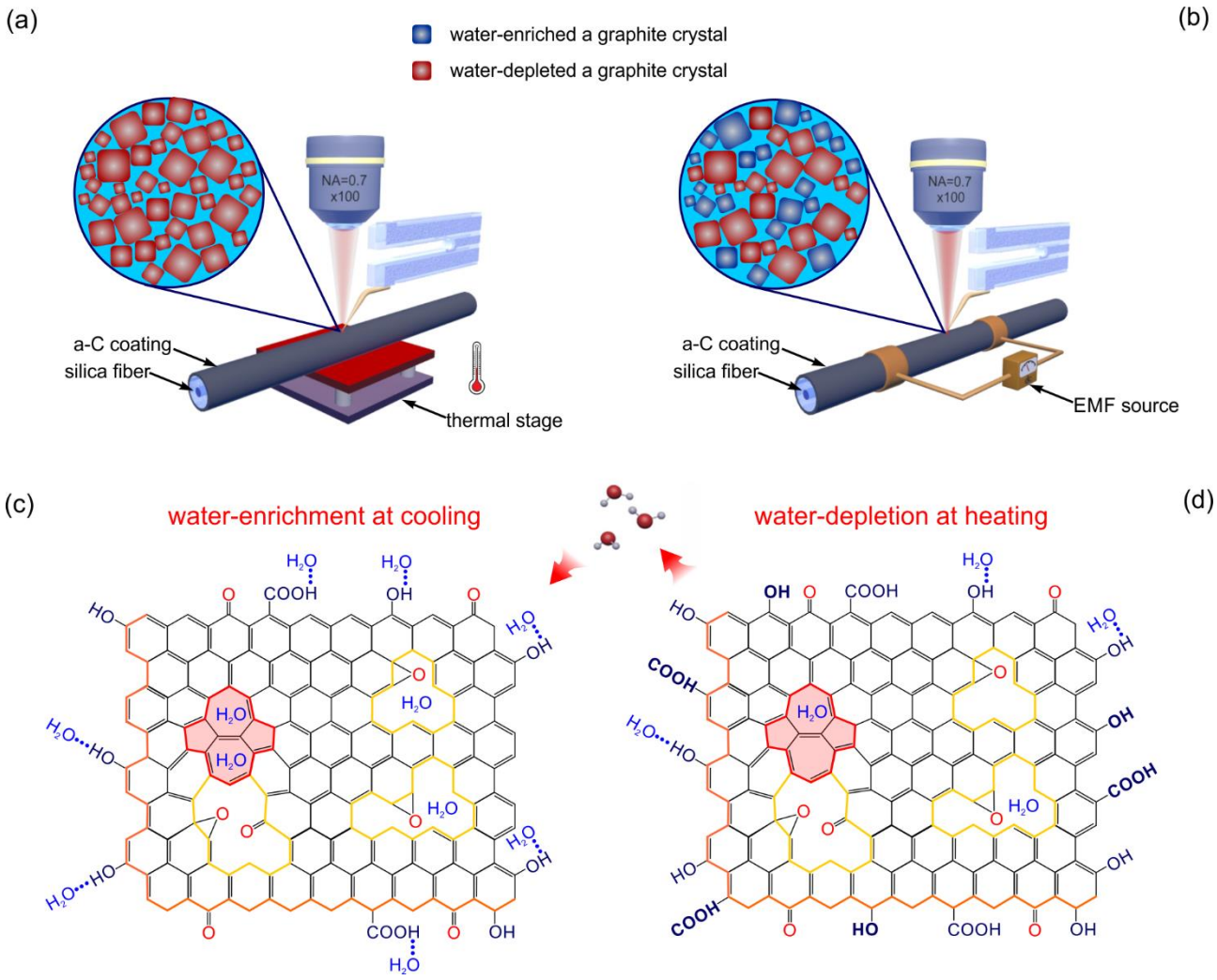

Figure 1. Schematic of experimental setups for thermal- (a) and electro- (b) assisted Raman spectroscopy and nanoscopy, sp^2 carbon sheets enriched (c) and depleted (d) with water directly interacting with structural defects and functional groups.

in which thermal and electrical heating/cooling of the carbon-coated fiber are implemented, respectively. The thermal scheme provides mild homogeneous annealing within the range of 30°C-150°C in air.

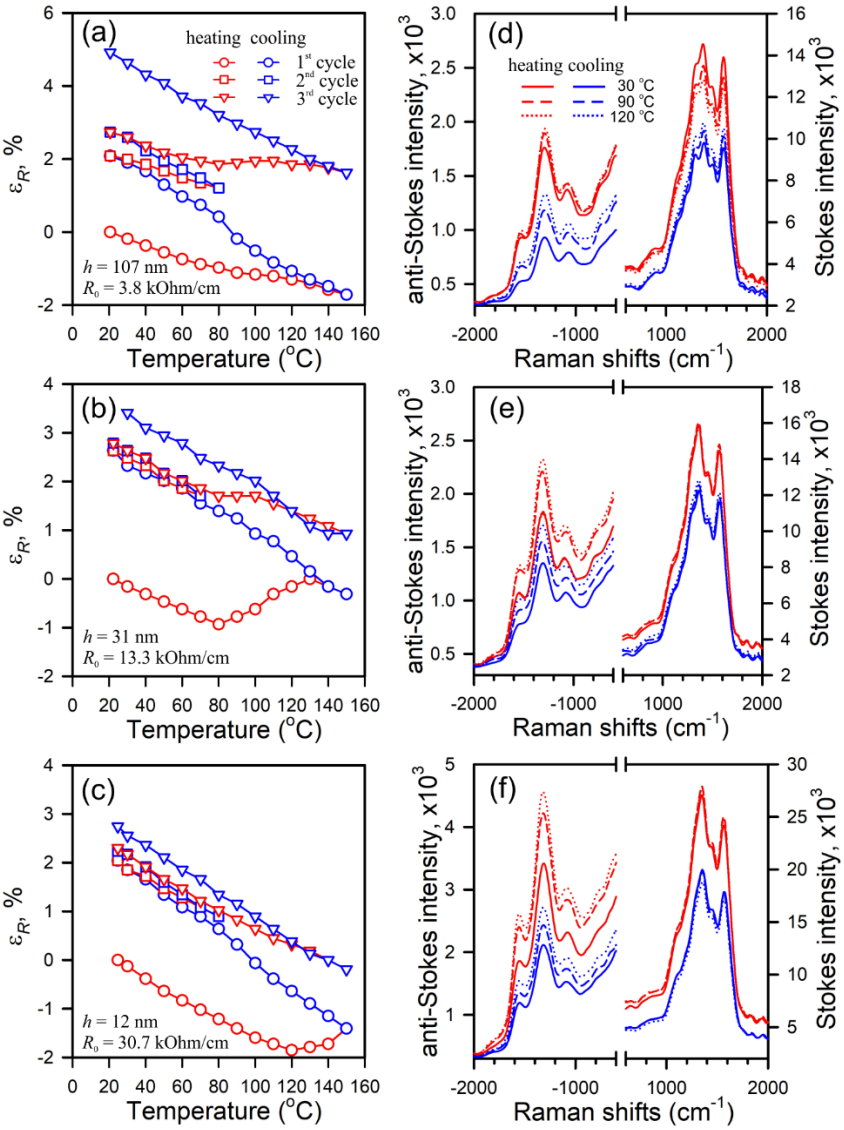

Figure 2. Relative change in the resistivity of a-C coatings having different thicknesses vs temperature in ambient air obtained using a hot plate, shown in Fig. 1 (a), (a)-(c), temperature-dependent anti-Stokes and Stokes Raman spectra captured for the same specimens.

In the electrical scheme version, the heating may be inhomogeneous due to percolation effects which enable extremely large local current densities at spots in which the neighboring crystals are in a direct contact. Fig. 1 (c) and (d) schematically illustrate the water-enrichment and -depletion of sp^2 graphene sheets containing structural/topological defects and functional groups when cooling and heating, respectively. A detailed analysis of the functionalization/defunctionalization of the defect-induced graphene sheets with H_2O molecules will be given below.

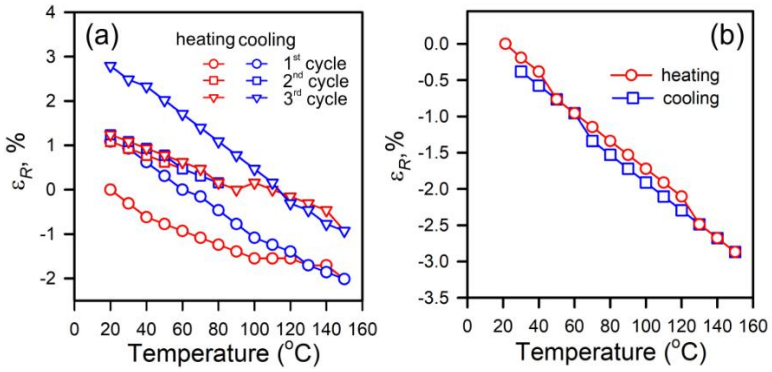

Figure 3. Relative change in resistance of the 31 nm a-C coating vs temperature: a) in air after mild annealing at 200°C and 10 mbar for 4 hours; b) in low vacuum environment with the pressure of 10 mbar. The results were obtained with the setup depicted in Fig. 1 (a).

Let us first consider the temperature-dependent behavior of the dc electrical resistance. All electric measurements were performed with a two-electrode scheme, as shown in Fig. 1 (b). At room temperature, their resistances, R_0, were found to be 30.7, 13.3 and 3.8 $k\Omega \cdot cm^{-1}$, respectively. To avoid imperfect ohmic contacts, both ends of the fiber specimens were galvanically coated, the coating length being 2 mm. A total length of the fiber specimen under study was ca. 14 mm. Figs. 2 (a)-(c) show the dependence of relative change in resistance, R, defined as:

$$\varepsilon_R = \frac{(R - R_0)}{R_0} \cdot 100\%, \qquad (2)$$

at multi-cyclic heating/cooling in air within the temperature range of 30°C-150°C. As expected, the a-C thin films exhibit a semi-conductive behavior. Below 80°C we see an almost linear and negatively sloped dependence of ε_R upon T. The heating above 80°C results in curving this dependence. The slope may change significantly and even become positive at certain temperatures, as for instance was observed for the 31 nm specimen (see Fig. 2 (b)). Such abnormality could be explained either by the rearrangement within the a-C domain system or by possible change in the

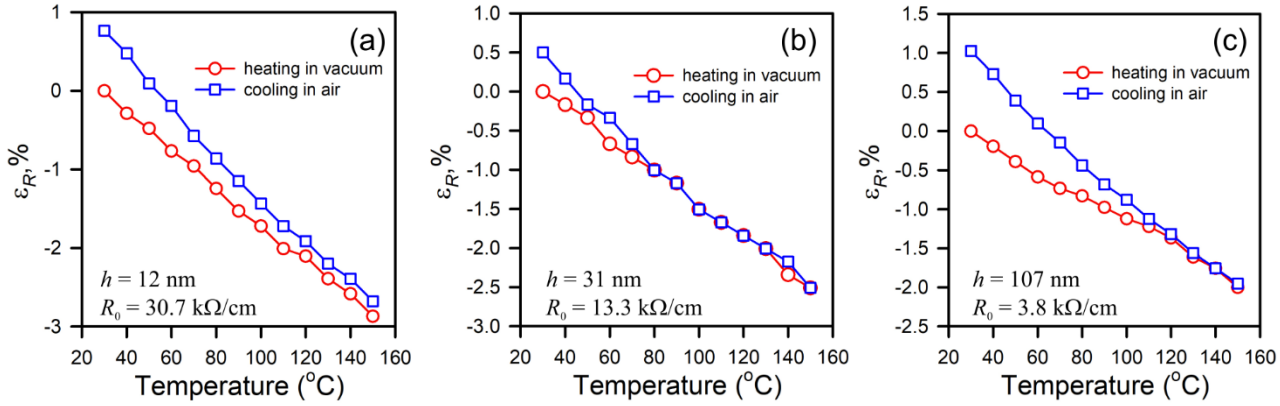

Figure 4. Relative change in resistivity vs temperature when heating and cooling are performed in low vacuum of 15 mbar and air, respectively, observed for the coating thicknesses: a) 12 nm, b) 31 nm and c) 107 nm. The results were obtained using the setup shown in Fig. 1 (a).

coating chemical composition. It is well established that the both processes are accompanied by releasing water from the samples at elevated temperatures and, eventually, the ultimate samples become hydrophobic.[20] Upon cooling down to room temperature we observe a hysteresis, which magnitude is about a few percent of the initial coating resistance (Fig. 2 (a)-(c)). Surprisingly, no hysteresis is observed upon the second excursion to 80°C and back (the 2nd cycle in Fig. 2(a)-(c)), whereas going beyond the temperature threshold shows the hysteresis again (the 3rd cycle in Fig. 2(a)-(c)). The observed effects are more significant for thicker carbon films. The hypothesis on rearrangements within the a-C domain system seems untenable since multiple heating and cooling

cycles should result in tamping the a-C coating, which would decrease the electrical resistance. To verify the above statement, we have first annealed the 31 nm a-C coated fiber at 200^{o}C for 4 hours in low vacuum at the pressure of 10 mbar and, then cooled the specimen down to room temperature. The resistance of the annealed specimen was then measured in ambient air upon heating and cooling, using the same as the above protocol. Fig. 3 (a) displays the behavior of the annealed specimen, which is quite similar to the one observed in Fig. 2(b). In another experiment, the same specimen was thermally cycled in low vacuum (10 mbar) conditions (Fig. 3(b)). Importantly, no resistance vs. temperature hysteresis was observed in the latter case. This result allows one to conclude that the resistance hysteresis is due to certain air species interacting with a-C and influencing its chemical composition.

To support this statement, we performed a series of somewhat different experiments. First, we heated the carbon-coated fibers in low vacuum up to 150^{o}C. After reaching the temperature of 150^{o}C, the vacuum oven was filled with air until the pressure equilibrated with the surrounding atmosphere. After that, the specimens were cooled down to the room temperature inside the oven. The results in Fig. 4 look pretty similar to those observed previously, when both heating and cooling were performed under the ambient air (Fig. 2 (a)-(c)). Upon the cooling, the ε_R vs. T slope increases gradually after passing through 80-120^{o}C region and, eventually, the resistance hysteresis appears (Fig. 4).

Thus, the presence of ambient air is found to be necessary for observing the resistance hysteresis. The logical next step is to identify the species responsible for such behavior. Among the components of ambient air, the most suspicious are oxygen and water. Multiple studies of interactions of graphite with oxygen showed that the oxidation becomes effective at much higher temperatures, normally exceeding 400°C.[31,32] Thus, we further attribute the observed changes to interactions between a-C and water, which is always present in ambient air.

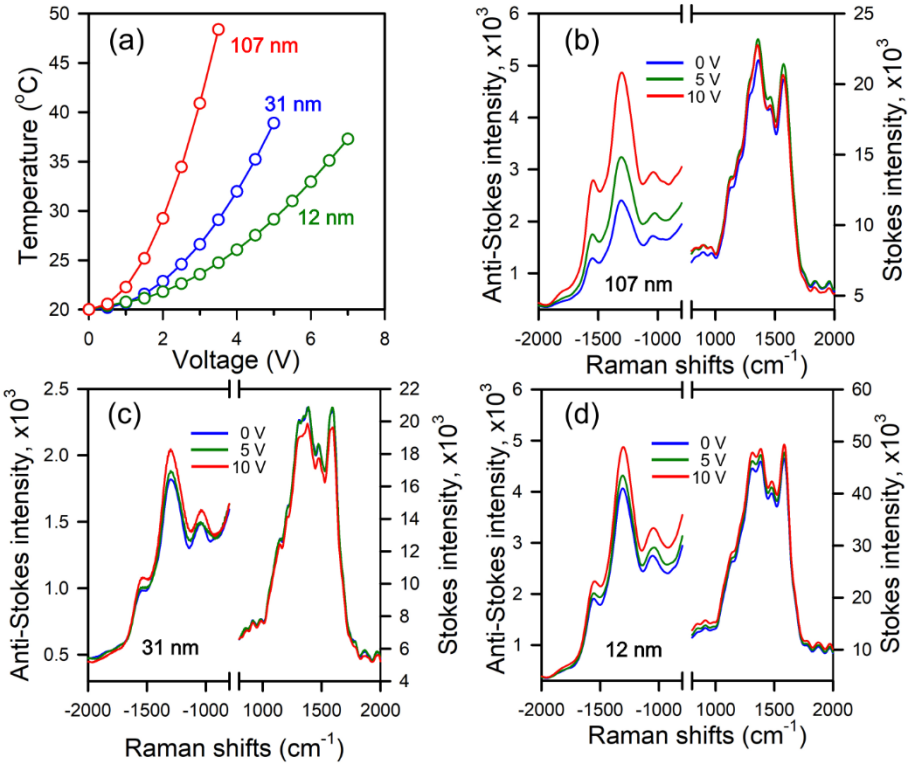

Figure 5. (a) Dependence of temperature of the a-C coating at an arbitrary spot upon the applied voltage. (b)-(d) Electro-assisted far-field Raman spectroscopy measurements for specimens having different thicknesses of the a-C coating.

The greatest hysteresis magnitude is observed for the 107 nm a-C coating (Fig 4 (c)), whereas the resistance hysteresis for the 31 nm film is somewhat less pronounced than that for the 12 nm specimen. This is explained by more intensive sorption of water by the smallest size crystals in the case of the 12 nm a-C coating. With increasing thickness, the average size of the crystals increases and the sorption activity decreases. It means that the thickness range of 30-60 nm corresponds to slower saturation of the a-C with water. This outcome is well consistent with our previous result by which the crystallinity degree, defined as G/D ratio, decreased with the thickness within the range of 30-60 nm.[26]

However, the temperature-controlled water-enrichment/depletion of the a-C crystals does not allow one to directly answer the question of how the resistance hysteresis occurs. We suppose that species of the intercalated water and species of water attached to the edge sites through hydrogen bonds are released from the a-C at the temperature above 80°C. Certain amount of water is capable of the dissociative absorption with the formation of additional functional groups at the edge defects.[20,21] Upon the cooling, water from the environment is gradually sorbed at the functionalized

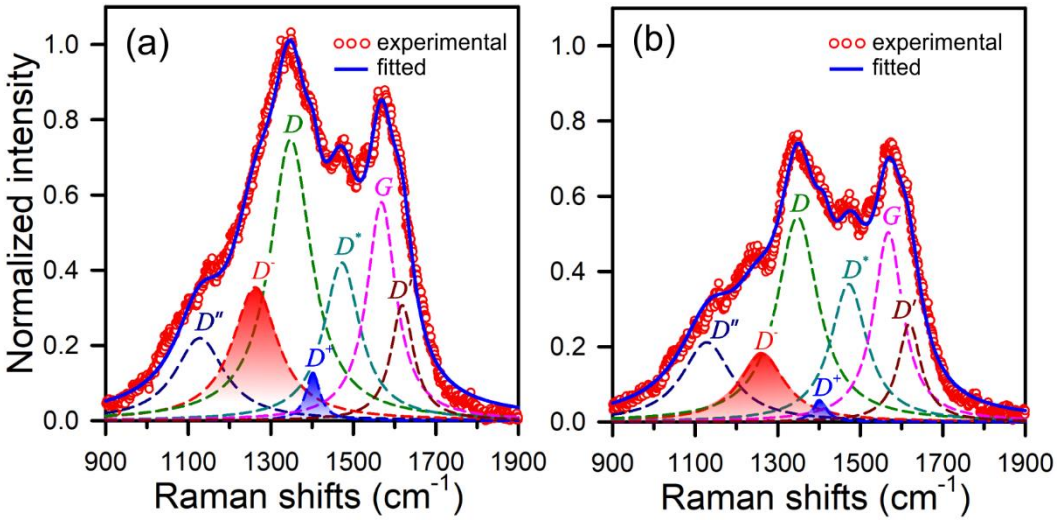

Figure. 6 Far-field Raman spectra of the 31 nm a-C coating collected at room remperature and decomposed into elementary peaks for two polarizations: (a) parallel and (b) perpendicular.

edge carbon atoms. The presence of H_2O molecules in the vicinity of graphene is known to increase the electrical resistance due to the opening of the band gap by the magnitude of up to 3.646 eV.[20] At each repeating heating/cooling cycle, the intercalated water irreversibly leaves the a-C crystal. As follows from Fig. 2(a)-(c), this effect depends upon the coating thickness. It seems to be reasonable to assume that thicker coatings require longer intercalated water depletion times. As was noted above, the oxidation of a-C at temperatures below 200°C is negligible. In order to run

this process, the temperature must exceed 400°C. The C-OH groups are also known to be thermally stable, at least up to 400°C.[33]

At the a-C surface, water is capable of dissociation, leading to formation of different functional groups, such as C-OH, C=O and C-H which interact with the edge carbon atoms at an energy barrier of ca. 0.7 eV (see Fig. 1 (c) and (d)).[34] Due to the presence of C-H moieties at the edge defects, hydroxyls and epoxy groups may react with hydrogen to produce H_2O molecules with a barrier of less than 0.15 eV.[35] The recent studies showed that the hydroxyls and carbonyls may react with each other to form a carboxyl group with an energy barrier of 0.31 eV.[21] All of the energy barriers are comparable to those to form hydrogen bonds that vary within the region of ca. 0.2 eV.[36]

The changes in chemical composition of the a-C are confirmed by anti-Stokes and Stokes Raman spectra taken at temperatures of 30°C, 90°C and 120°C, as shown in Fig. 2 (d)-(f). For convenience, all spectra were smoothened with the regularized singular value decomposition method. We observe the enhancement of a new Raman peak at 1260 cm^{-1} in the *D*-region of the Raman spectra with increasing the film thickness. On passing through 150°C, the intensity of Raman spectra experiences a jump down due to changes in the morphology of the a-C coating. A careful examination of the Raman spectra indicates the existence of a temperature hysteresis observed during the heating/cooling cycles. Indeed, at any spot of the carbon coating, the temperature can be determined using the following relationship:[37]

$$T = \frac{\hbar c \Omega}{k_B \ln\left[\frac{I_s}{I_{as}} \frac{\sigma_{as}}{\sigma_s} \left(\frac{\omega_0 + \Omega}{\omega_0 - \Omega}\right)^4\right]}, \quad (3)$$

where $I_s\,(\sigma_s)$ and $I_{as}\,(\sigma_{as})$ are Stokes and anti-Stokes intensities (cross-sections), respectively, ω_0 is the excitation frequency, Ω is a phonon frequency, $\hbar$ is the Planck constant, c is the speed of light, k_B is the Boltzmann constant. As follows from Fig. 2 (d)-(f), the temperature, determined via

Eq. (3), changes uniformly upon the heating, whereas it decays slower upon the cooling. This effect is caused by the irreversible intercalated water depletion and the functionalization of the edge defects with water. At thermal mild annealing (see Fig. 1(a)) this functionalization proceeds uniformly throughout the sample. The photo-heating of the a-C exposed to the incident 632.8 nm (1.96 eV) laser light is negligible. In the case of the electro-heating, as depicted in Fig. 1(b), the a-C coating is heated non-uniformly due to the percolation effects. It means that at hot spots, where

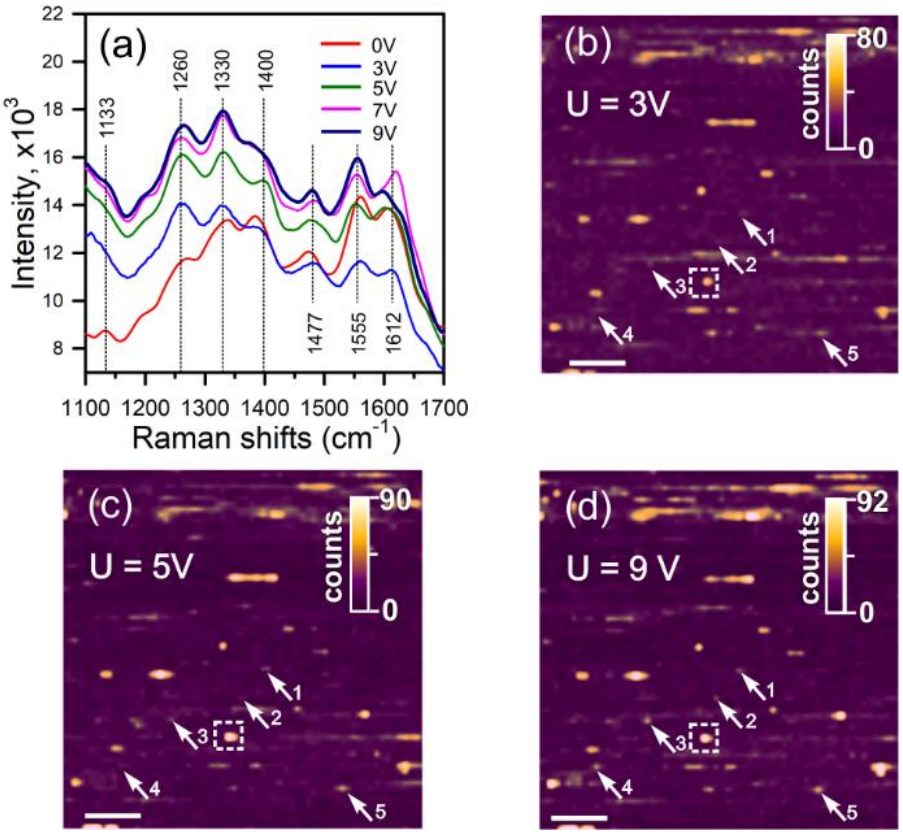

Figure 7. (a) TERS spectra of the 31 nm a-C coating exposed to applied voltage. (b)-(d) TERS maps at 1260 cm^{-1} for different voltages (the bar is 500 nm). The hot spots on the TERS maps are highlighted with the numbers 1 to 5.

the conducting crystals are in contact with each other, the local current density may reach larger magnitudes. Scanning thermal microscopy allows one to probe the temperature as a function of

applied voltage at an arbitrary spot at the surface of the a-C, as shown in Fig. 5 (a). As expected, these curves are perfectly fitted with parabolic functions. Despite the modest changes in temperature, the SThM cantilever undergoes large bending deformations and as a consequence it becomes difficult to support the feedback at larger voltages. Based on this fact, we conclude that the a-C coating is heated non-uniformly. A mild heating is confirmed by electro-assisted far-field Raman spectroscopy, as shown in Fig. 5 (b)-(d). It is easy to monitor changes in the structure of *D*-region in which a new specific Raman band at 1260 cm^{-1} is clearly observed. Unlike the thermal annealing (see Figs. 2 (d)-(f)), the electro-heating facilitates the water-depletion of the a-C coating at the hot spots and the water-enrichment of the colder a-C crystals, as schematically illustrated in Fig. 1 (b). This is why the edge sites are intensively anchored with water through the hydrogen bonding mechanism. Thus, thermal- and electro-assisted Raman spectroscopy clearly indicate the appearance of the new Raman peak within the *D*-region that could be potentially assigned to carboxyl and/or hydroxyl groups. To evidence this hypothesis, we utilized polarization-controlled Raman spectroscopy and as-registered Raman spectra were deconvoluted using a regularized least-square fitting approach. All individual peaks were assumed to be Lorentzian functions. Fig. 6 shows normalized Raman spectra of the 31 nm a-C coating at room temperature and their decomposition into elementary components in the parallel (a) and perpendicular (b) polarizations with the correlation of 0.998 and 0.997, respectively. The peak positions and the full widths at half height (FWHH) to decompose the 'perpendicular' spectrum (Fig. 6 (b)) were taken from the as-calculated 'parallel' spectrum (Fig. 6(a)). We observe a noticeable rearrangement of the intensity of two low(D^-)- and high(D^+)-frequency Raman bands at 1260 cm^{-1} and 1400 cm^{-1}. The latter peak is relatively small, but was introduced due to its enhancement in a TERS spectrum, as will be shown below. The calculated depolarization ratios for all 7 bands were found to be $\rho_{D''} = 0.96$, $\rho_{D^-} = 0.50$, $\rho_D = 0.72$, $\rho_{D^+} = 0.43$, $\rho_{D^*} = 0.87$, $\rho_G = 0.85$ and $\rho_{D'} = 0.95$. Both the D' and D''

bands are partially polarized and correspond to full-symmetric vibrational modes. Early theoretical works showed that the $D^{\pm}$ bands can be attributed to the hydroxyl groups, which are commonly polarized.[24] As higher temperatures, achieved via either thermal or electro-heating, the amount of the water-anchored hydroxyl groups is reduced and only the water-free hydroxyl groups contribute

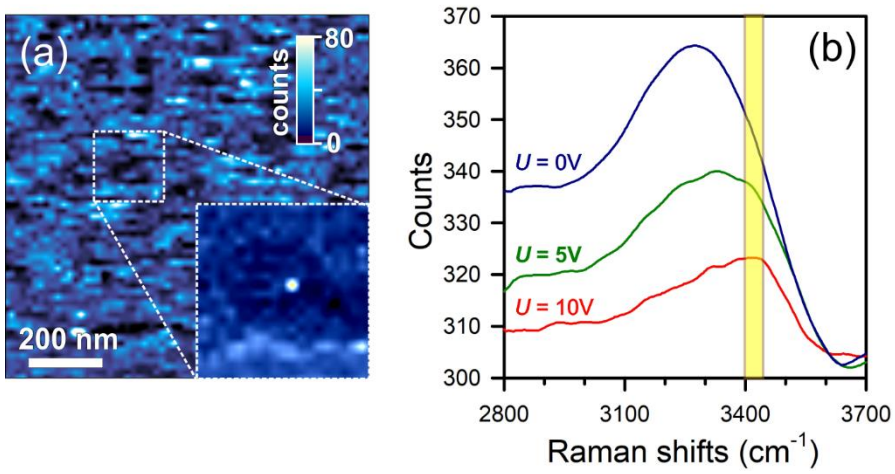

Figure 8. (a) TERS map of the 31 nm a-C coating at 3420 cm^{-1} at zero voltage and room temperature. (b) TERS spectra of the 31 a-C coating within the spectral range of 2800-3700 cm^{-1} at different voltages.

to the spectra. This effect is ideally recognized with electro-assisted TERS spectroscopy and nanoscopy. Due to the tight localization of the incident light with the help of a gold tip the inelastically-scattered light becomes coherent[38,39] and the proper Raman bands narrow. Fig. 7 (a) displays TERS spectra of the 31 nm a-C at different applied voltages. These spectra were taken from the area marked with a dashed square in Figs. 7 (b)–(d). As expected, a local electro-heating leads to the intensity enhancement of the $D^{\pm}$ bands and it is satisfactorily consistent with the appearance of water-free hydroxyl groups. A red-shift of the *G* band to 1555 cm^{-1} is related to the enhancement of the amorphous species rather than the expansion of the sp^2 carbon domains.[40] The hot spots on the TERS maps captured at 1260 cm^{-1} are highlighted with the numbers 1 to 5 in Fig.

7 (b)-(d). At electro-heating, some of the functionalized defect sites become water-depleted and, therefore their relative intensities increase. A direct visualization of water-enriched domains is demonstrated on a TERS map taken at 3420 cm^{-1} where one of the domains is given in the inset with the improved spatial resolution. The electro-assisted TERS spectra within the spectral range of 2800-3700 cm^{-1} are shown in Fig. 8 (b). These spectra indicate the water-depletion of the a-C with increasing voltage. Thus, we conclude that the edge defects are commonly anchored with water through the hydrogen bonds. Such defects become water-free upon mild annealing at the temperature not exceeding 200^{o}C.

Concluding remarks

In this paper, we evidenced the presence of water-anchored edge defects in amorphous carbon coatings by unraveling an anomalous behavior of the dc electrical resistance and resolving the highly overlapped *D*-family bands in polarization-controlled Raman and TERS spectroscopy and nanoscopy. We claim that the resistance hysteresis is related to partial dissociation of intercalated water from a-C and formation of water-functionalized edge defects at temperature of above 80^{o}C. This hypothesis has been supported by the appearance of new Raman bands at 1260 cm^{-1} and 1400 cm^{-1}, attributed to the COOH/C-OH groups, as have been predicted in previous studies.[20,24] Functionalization of COOH/C-OH groups with water through hydrogen bonding allows one to understand the rearrangement of the *D*-family bands. A straightforward visualization of water-enriched domains of a-C with the electro-assisted TERS spectroscopy and nanoscopy at 3420 cm^{-1} provides a clear evidence for the existence of water-anchored edge defects. We believe our studied be beneficial in understanding the water/a-C interactions, which would further help to improve the performance of carbon coatings in harsh environments.

METHODS

Sample preparation

All optical silica fibers under study were drawn at OFS. The a-C coatings were deposited via thermal CVD using the same hydrocarbon as precursor. The a-C coating thickness was controlled by either the fiber draw speed or the precursor gas flow rate. Initially, the fibers were manufactured with an acylate coating on top of the carbon layer. Prior to further analyses, the acrylate material was removed from fiber specimens by immersing them in hot sulfuric acid.

Dc electrical resistance measurements

The surface dc conductivity was probed in contact mode by applying voltage to the sample with the help of the atomic force microscopy (AFM) microscope NTEGRA PRIMA™ (NT-MDT). As a probe, we used conducting AFM cantilevers CSG1-/Pt (NT-MDT). A distance between the AFM cantilever, referred to as a working electrode, and a counter electrode connected to upper surface was about 2 mm. Tip-sample force was typically in the range of 10-15 nN during measurements. Unless specified in the text, the resistance measurements were performed in ambient air. The relative humidity in the lab was in the range 30-50% and was not specifically controlled, thus it might vary from one sample to another.

Scanning thermal microscopy

Thermal measurements were performed with the SThM setup (AU040 unit, NT-MDT) using a specialized SThM_P probe (NT-MDT). A tip apex of the probe is a NiCr/Pd resistor with a curvature radius of <100 nm. The instrumental error is on the order of 0.1 °C.

Tip fabrication for TERS measurements

Gold tips for TERS measurements were fabricated from a 75 μm gold wire (purity: 99.99%, Goodfellow). It was immersed in a mixture of fuming hydrochloric acid (HCl, 37%) and ethanol

[C_2H_5OH, 96%] in a volume proportion of 1:1. The tapering was performed using adaptive dc-pulsed electrochemical etching with a self-tunable duty cycle and working potentials of V_b = 1.8 V and V_{up} = 2.1 V. Upon achieving the current cutoff event, the tips were safely retracted from the solution surface with a piezo-manipulator and were immediately rinsed with distilled water and dried with nitrogen. The curvature radii of the gold tips were estimated to be within the range of 20-30 nm. The as-prepared gold tips were exposed to bending and then glued to a long tab of a near-horizontally oriented tuning fork TF103_NTF (NT-MDT) operating at the resonance frequency of 32 kHz.

Far- and near-field Raman spectroscopy and nanoscopy

Far-field and near-field Raman spectra and maps were captured with a multi-purpose analytical instrument NTEGRA SPECTRA™ (NT-MDT) in upright configuration. This represents a confocal Raman spectrometer equipped with a scanning probe microscope. The spectrometer was wavelength calibrated with a silicon wafer by registering a first-order Raman band centered at 520 cm^{-1}. A sensitivity of the spectrometer was as high as ca. 2500 photon counts per 0.1 s provided that we used a 100×objective (N.A.=0.7), an exit slit of 100 μm and a linearly polarized light with the wavelength of 632.8 nm and the power at the sample of 5.6 mW. No signal amplification regimes of a Newton EMCCD camera (ANDOR, Ireland) was applied.

A sample of interest was exposed to a laser light with the wavelength of 632.8 nm and the intensity of 1 kW/cm^2. The tip does near-vertical oscillations at the distance of 2-3 nm above the sample. A signature of the surface localized plasmon based field enhancement beneath the apex gold tip was the rotation of a two-lobe Rayleigh scattering pattern at the focal plane when turning the linear polarization direction. 128x128 pixel TERS maps were raster scanned with a step of 10 nm and an exposure time per pixel of 0.1 s and were finally collected with the EMCCD camera

cooled down to -100°C. Far- and near-field Raman spectra within the range of 200-2000 cm^{-1} were registered with spectral resolution of 3 cm^{-1} using a 600 grooves/mm grating.

Corresponding Author

*Dr. Sergey S. Kharintsev, email: Sergey.Kharintsev@kpfu.ru, tel.: +7(843)2337741

Notes

The authors declare no competing financial interest.

This work was supported by grant No. 19-12-00066 of the Russian Science Foundation. We are very grateful to Dr. A.M. Dimiev (Kazan Federal University), Dr. A.V. Kharitonov (Kazan Federal University) and Dr. A.R. Gazizov (Kazan Federal University) for invaluable discussion and critical remarks. This work was done using equipment of Federal Center of Shared Facilities of Kazan Federal University.

Graphical TOC Entry

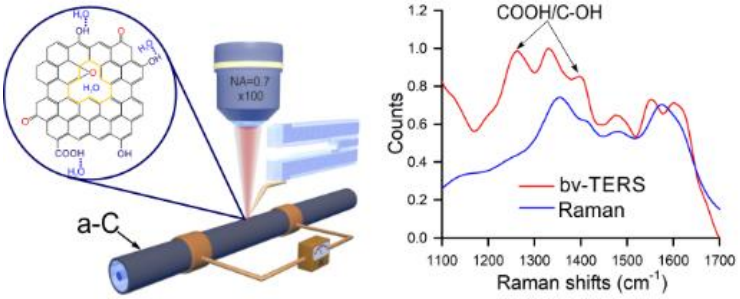

References

1. Lemaire, P. J.; Lindholm, E. A. Hermetic Optical Fibers: Carbon-Coated Fibers. In *Specialty Optical Fibers Handbook;* Mendez, A., Morse, T. F., Eds.; Elsevier Academic Press: Burlington, **2007**; pp 453–490.
2. Allsop, T.; Neal, R. A Review: Evolution and Diversity of Optical Fibre Plasmonic Sensors. *Sensors* **2019**, *19*, 1–19.
3. Shiue, S. T.; He, J. L.; Pan, L. Y.; Huang, S. T. Thermally Induced Stress Voids in Hermetically Carbon-Coated Optical Fibers with Different Coating Thickness. *Thin Solid Films* **2002**, *406*, 210–214.
4. Kudin, K. N.; Ozbas, B.; Schniepp, H. C.; Prud'homme, R. K.; Aksay, I. A.; Car, R. Raman Spectra of Graphite Oxide and Functionalized Graphene Sheets. *Nano Lett.* ***2008***, *8*, 36–41.
5. *Beams, R.; Cançado, L. G.; Novotny, L. Raman characterization* of *Defects* and *Dopants* in *Graphene*. *J. Phys.: Condens. Matter*. ***2015***, *27*, 1–26.
6. *Geim, A. K.; MacDonald, A. H. Graphene: Exploring Carbon Flatland*. *Phys*. *Today* **2007**, *60*, 35–41.
7. *Biroju, R. K.; Rajender, G.; Giri, P. K.* On the *Origin* and *Tunability* of *Blue* and *Green Photoluminescence* from *Chemically Derived Graphene: Hydrogenation* and *Oxygenation Studies. Carbon N.Y.* ***2015***, *95, 228−238.*
8. Dresselhaus, M. S.; Dresselhaus, G.; Saito, R.; Jorio, A. Raman Spectroscopy of Carbon Nanotubes. *Phys. Rep.* **2005**, *409*, 47–99.
9. Kronto, H. W.; *Heath, J. R.; O'Brien, S. C.; Curl, R. F.; Smalley, R. E.* C60: Buckminsterfullerene. *Nature* **1985**, *318*, 162–163.
10. Sasaki, K.; Sekine, Y.; Tateno, K.; Gotoh, H. Topological Raman Band in the Carbon Nanohorn. *Phys. Rev. Lett.* **2013**, *111*, 1–5.

11. Dervishi, E.; Ji, Z.; Htoon, H.; Sykora, M.; Doorn, S. K. Graphene Quantum Dots : Size and Structure Dependence. *Nanoscale* **2019**, *35*, 16571–16581.
12. Dunlap, B. I. Relating Carbon Tubules. *Phys. Rev. B* **1994**, *49*, 5643–5651.
13. Fotopoulos, N.; Xanthakis, J. P. Electronic structure of SP^2 Trap States in Amorphous Carbon. *Surf. Interface Anal.* **2007**, *39*, 132–134.
14. Robertson, J. Amorphous Carbon. *Adv. Phys.* **1986**, *35*, 317–374.
15. Curran, S. A.; Talla, J. A.; Zhang, D.; Carroll, D. L. Defect-Induced Vibrational Response of Multi-Walled Carbon Nanotubes Using Resonance Raman Spectroscopy. *J. Mater. Res.* **2005,** *20*, 3368–3373.
16. Hashimoto, A.; Suenaga, K.; Gloter, A.; Urita, K.; Iijima, S. Direct Evidence for Atomic Defects in Graphene Layers. *Nature* **2004**, *430*, 870–873.
17. Fujimori, T.; Urita, K.; Ohba, T.; Kanoh, H. Evidence of Dynamic Pentagon - Heptagon Pairs in Single-Wall Carbon Nanotubes using Surface-Enhanced Raman Scattering. *J. Am. Chem. Soc*. **2010**, *139*, 6764–6767.
18. Sun, P. Z.; Yang, Q.; Kuang, W. J.; Stebunov, Y. V.; Xiong, W. Q.; Ju, J.; Nair, R. R.; Katsnelson, M. I.; Yuan, S. J.; Grigorieva, I. V; Lozada-Hidalgo, M.; Wang, F. C.; Geim, A. K. Limits on Gas Impermeability of Graphene. *Nature* **2020**, *579*, 229-232.
19. Ghaderi, N.; Peressi, M. First-Principle Study of Hydroxyl Functional Groups on Pristine, Defected Graphene, and Graphene Epoxide. *J. Phys. Chem. C* **2010**, *114*, 21625–21630.
20. Xu, Z.; Ao, Z.; Chu, D.; Younis, A.; Li, C. M.; Sean, Li. Reversible Hydrophobic to Hydrophilic Transition in Graphene via Water Splitting Induced by UV Irradiation. *Sci. Rep.* **2014**, *4*, 1–10.
21. Sun, P.; Wang, Y.; Liu, H.; Wang, K.; Wu, D.; Xu, Z.; Zhu, H. Structure Evolution of Graphene Oxide during Thermally Driven Phase Transformation: Is the Oxygen Content Really Preserved? *PLoS ONE* **2014**, *9*, 1–8.

22. Jia, X.; Hofmann, M.; Meunier, V.; Sumpter, B. G.; Campos-Delgado, J.; Romo-Herrera, J. M.; Son, H.; Hsieh, Y. P.; Reina, A.; Kong, J.; Terrones, M.; Dresselhaus, M. S. Controlled Formation of Sharp Zigzag and Armchair Edges in Graphitic Nanoribbons. *Science* **2009**, *323*, 1701–1705.
23. Mattevi, C.; Eda, G.; Agnoli, S.; Miller, S.; Mkhoyan, K. A.; Celik, O.; Mastrogiovanni, D.; Granozzi, G.; Garfunkel, E.; Chhowalla, M. Evolution of Electrical, Chemical, and Structural Properties of Transparent and Conducting Chemically Derived Graphene Thin Films. *Adv. Funct. Mater.* **2009**, *19*, 2577–2583.
24. Rajender, G.; Giri, P. K. Formation Mechanism of Graphene Quantum Dots and Their Edge State Conversion Probed by Photoluminescence and Raman Spectroscopy. *J. Mater. Chem. C* **2016**, *4*, 10852–10865.
25. Sadezky, A.; Muckenhuber, H.; Grothe, H.; Niessner, R.; Poschl, U. Raman Micro Spectroscopy of Soot and Related Carbonaceous Materials: Spectral Analysis and Structural Information. *Carbon* **2005**, *43*, 1731–1742.
26. Kharintsev, S. S.; Saparina, S. V.; Stolov, A. A.; Li, J.; Fishman, A. I. Sensing Carbon Allotropes in Protective Coatings on Optical Fibers with Far- and Near-field Raman Spectroscopy and Microscopy. *J. Raman Spectrosc.* **2017**, *48*, 1346–1355.
27. Claramunt, S.; Varea, A.; Lopez-Diaz, D.; Velazquez, M. M.; Cornet, A.; Cirera, A. The Importance of Interbands on the Interpretation of the Raman Spectrum of Graphene Oxide. *J. Phys. Chem. C* **2015**, *119*, 10123–10129.
28. Tuinstra, F.; Koenig, J. L. Raman Spectrum of Graphite. *J. Chem. Phys.* **1970**, *53*, 1126–1130.
29. Rebelo, S. L. H.; Guedes, A.; Szefczyk, M. E.; Pereira, A. M.; Araujo, J. P.; Freire, C. Progress in the Raman Spectra Analysis of Covalently Functionalized Multiwalled Carbon Nanotubes: Unraveling Disorder in Graphitic Materials. *Phys. Chem. Chem. Phys.* **2016**, *18*, 12784–12796.

30. Stolov, A. A.; Lombardo, J. J.; Slyman, B. E.; Li, J.; Chiu, W. K. S. Carbon Coatings on Silica Glass Optical Fibers Studied by Reflectance Fourier-transform Infrared Spectroscopy and Focused Ion Beam Scanning Electron Microscopy. *Thin Solid Films* **2012**, *520*, 4242–4248.
31. Xiaowei, L.; Jean-charles, R.; Suyuan, Y. Effect of Temperature on Graphite Oxidation Behavior. *Nucl. Eng. Des.* **2004**, *227*, 273–280.
32. Hahn, J. R. Kinetic Study of Graphite Oxidation along Two Lattice Directions. Carbon **2005**, *43*, 1506–1511.
33. Ganguly, A.; Sharma, S.; Papakonstantinou, P.; Hamilton, J. Probing the Thermal Deoxygenation of Graphene Oxide Using High-Resolution In Situ X-ray-Based Spectroscopies. *J. Mater. Chem. C* **2011**, *115*, 17009–17019.
34. Buchsteiner, A.; Lerf, A.; Pieper, J. Water Dynamics in Graphite Oxide Investigated with Neutron Scattering. *J Phys Chem B* **2006**, *110*, 22328–22338.
35. Kim, S.; Zhou, S.; Hu, Y.; Acik, M.; Chabal, Y. J.; Berger, C.; de Heer, W.; Bongiorno, A.; Riedo, E. Room-Temperature Metastability of Multilayer Graphene Oxide Films. *Nat. Mater.* **2012**, *11*, 544–549.
36. *Goss*, J. P.; Jones, R.; Heggie, M. I.; Ewels, C. P.; Briddon, P. R.; Öberg, S. *Theory of Hydrogen in Diamond*. *Phys. Rev. B* **2002**, *65*, 1–14.
37. *Baibarac, M.; Baltog*, I.; *Matea*, A.; Mihut, L.; *Lefrant, S.* Anti-Stokes Raman Spectroscopy as a Method to Identify the Metallic and Semiconducting Configurations of Double-Walled Carbon Nanotubes. *J. Raman Spectrosc.* **2015**, *46*, 32–38.
38. *Cançado*, L. G.; Jorio, A.; Ismach, A.; Joselevich, E.; Hartschuh, A.; Novotny *L.* Mechanism of Near-Field Raman Enhancement in One-Dimensional Systems. *Phys. Rev. Lett.* **2009**, *103*, 1–4.
39. Canado, L. G.; Beams, R.; Jorio, A.; Novotny, L. Theory of Spatial Coherence in Near-Field Raman scattering. *Phys. Rev. X* **2014**, *4*, 1–14.

40. *Botella, P.; Devaux, X.; Dossot, M.; Garashchenko*, V.; *Beltzung*, J. G.; *Soldatov*, A. V.; Ananev, S. *Single-Walled Carbon Nanotubes Shock-Compressed* to *0.5 Mbar*. *Phys. Status Solidi B* **2017**, *254*, 1–6.